Available online at www.sciencedirect.com
ScienceDirect
Trans. Nonferrous Met. Soc. China 30(2020) 872−882
Transactions of Nonferrous Metals Society of China
www.tnmsc.cn

Effect of Al_3Zr particles on hot-compression behavior and processing map for Al−Cu−Li based alloys at elevated temperatures

Qing-bo YANG[1], Yan-jun DENG[2], Mou YANG[1], Zhi-qing ZHANG[1,3,4], Wei-guo LI[5], Qing LIU[1]

1. College of Materials Science and Engineering, Chongqing University, Chongqing 400045, China;
2. Chang'an Auto Global R&D Center, Chongqing 401120, China;
3. China Xipeng Aluminum Industrial Park, Chongqing 401326, China;
4. Chongqing University−University of Cincinnati Joint Co-op Institute, Chongqing University, Chongqing 401331, China;
5. College of Aerospace Engineering, Chongqing University, Chongqing 400045, China

Received 11 June 2019; accepted 17 February 2020

Abstract: The influence of Al_3Zr particles on the hot compression behavior and processing map (PM) of Al−Cu−Li based alloys under isothermal plane-strain compression in the temperature range of 400−500 °C and at the strain rates of 0.01−10 s^{-1} was investigated. The corresponding microstructure was analyzed using optical microscopy (OM), electron back-scattered diffraction (EBSD) and transmission electron microscope (TEM). The results showed that dynamic recovery (DRV) played a greater role than dynamic recrystallization (DRX) in dynamic softening. At low temperatures, the Al_3Zr particles were the significant barriers to inhibit DRV and DRX grain growth. When the temperature reached 500 °C, the Al_3Zr particles readily spread along grain boundaries just like a necklace due to the dissolution of Al_3Zr particles and rapid diffusion of Zr through grain boundary, resulting in generating the macroscopic cracks and forming an instability domain at 490−500 °C, 0.01 s^{-1} in the PM.

Key words: Al−Cu−Li based alloy; Al_3Zr particle; hot compression; processing map

1 Introduction

The ongoing thrust in aerospace applications has caused the rapid development of lightweight structural materials such as Al−Cu−Li based alloys in recent years. Lithium is the lightest metallic element, having the advantages of reducing the mass of aerospace structural components. For example, 1 wt.% Li addition decreases by 3% in density approximately, and enhances by 6% in elastic modulus of Al alloys, contributing to high strength/fracture toughness, fatigue resistance and corrosion resistance of the materials [1,2]. Therefore, the family of Al−Cu−Li based alloys like AA2195 aluminum alloy has been widely tailored to apply to a variety of structural components for aerospace systems, such as cryogenic propellant tanks and large aircraft shells, owing to its lower density, higher strength, better malleability and weldability, and smaller anisotropy [2,3].

To manufacture these components and meet the strict requirements for their microstructure and mechanical properties, different processing procedures including hot extrusion, rolling and forging are adopted. Generally, the microstructure and mechanical properties during hot working are predominately controlled by the deformation

Foundation item: Project (11727802) supported by the National Natural Science Foundation of China; Projects (2018CDJSK04XK09, 106112017CDJQJ328840) supported by the Fundamental Research Funds for the Central Universities, China
Corresponding author: Zhi-qing ZHANG; Tel: +86-2365102016; E-mail: zqzhang@cqu.edu.cn
DOI: 10.1016/S1003-6326(20)65261-X

parameters which are able to be analyzed and optimized using the processing map (PM) in the light of dynamic materials modeling (DMM). To identify and optimize the deformation parameters, PM is applied in validating the deformation mechanisms in the hot compression process of Al−Cu−Li based alloys.

In general, the Zr element in AA2195 aluminum alloy can improve the thermal stability of the alloys since the Zr element inhibits the recrystallization through the formation of coherent $L1_2$ structured Al_3Zr particles [4,5−7]. However, as the temperature rose to ~475 °C in the aging treatment process, the metastable Al_3Zr phases were relatively unstable in Al−Zr alloys [6,8]. Moreover, the Al_3Zr ($L1_2$) precipitates coarsened into equilibrium Al_3Zr ($D0_{23}$) phases under overage condition (aging at near 500 °C) for Al−0.1Zr−0.1Ti (at.%) alloys [9]. The tetragonal Al_3Zr ($D0_{23}$) phases that were the inherent brittleness could not afford enough equivalent slip systems to coordinate the deformation of the Al matrix [10].

Previous investigations of Al alloys indicated that Al_3Zr particles could exist at 300−500 °C during hot deformation [11]. At low temperatures (300−450 °C), the Al_3Zr particles effectively inhibited the process of dynamic recrystallization (DRX) and dynamic recovery (DRV), owing to the enhanced pinning effects on grain boundary migration and dislocation motion [12]. However, few studies have focused on the impact of Al_3Zr particles on hot-compression behavior and the PM of AA2195 aluminum alloy at elevated temperatures (450−500 °C).

In general, the occurrence of DRX in Al−Cu−Li based alloys is more often found at high temperature condition. Table 1 exhibits the optimized stable domain in the PMs applied in 2xxx series aluminum alloys. It can be seen that the optimized processing temperatures for the 2xxx series alloys during the hot-compression deformation are around 500 °C [13−19]. After hot deformation, the hot-formed specimens will be subjected to different aging treatments to obtain better mechanical properties for aerospace structural components. Therefore, it is necessary to systematically understand whether Al_3Zr particles coarsen or transform into equilibrium Al_3Zr ($D0_{23}$) phases or dissolve into the matrix at the elevated temperatures because these changes reduce the thermal stability of AA2195 aluminum alloy.

Table 1 Optimized stable domain in PMs applied in 2xxx series aluminum alloys

No.	Alloy	Optimized stable region	Ref.
1	W049	475 °C, 5×10^{-4} s^{-1}	[13]
2	UL40	475 °C, 0.1 s^{-1}	[14]
3	2060	380−500 °C, 0.01−3 s^{-1}	[15]
4	2219	380−510 °C, 0.008−0.78 s^{-1}	[16]
5	2195	475−525 °C, 0.1−1 s^{-1}	[17]
6	Al−Cu−Li−Zr−Sc	460−500 °C, 0.001−0.1 s^{-1}	[18]
7	Al−Cu−Li−Zn−Mg−Mn−Zr	450−500 °C, 0.01−0.1 s^{-1}	[19]

In this work, the influence of Al_3Zr particles on hot compression behavior of AA2195 aluminum alloy during isothermal plane-strain compression at elevated temperatures (450−500 °C) was investigated and discussed in detail by flow stress curves, PM and microstructure characterization.

2 Experimental

In this study, AA2195 aluminum alloy sheets with the nominal chemical composition of 93.91 Al, 1.02 Li, 4.12 Cu, 0.4 Ag, 0.44 Mg, 0.11 Zr (wt.%) were used. The cuboid samples (20 mm × 15 mm × 10 mm) machined through the wire-cut process from the central part of the plate were subjected to homogenization treatments at (440 °C, 16 h) + (490 °C, 20 h) in the hot furnace with an air circulating system. The homogenized specimens were then subjected to the water quenching process. The homogenized AA2195 aluminum alloy mainly consists of the equiaxed grains with the size of ~150 μm, as shown in Fig. 1.

To simulate the hot rolling process, the Gleeble−3500 apparatus was employed to perform plane-strain compression tests under different compression conditions (400−500 °C, 0.01−10 s^{-1}). All specimens were coated with graphite lubricant to reduce friction. The specimens were isothermally compressed at different desired test temperatures with the heating speed of ~5 °C/s and kept isothermally under this condition for 3 min, and

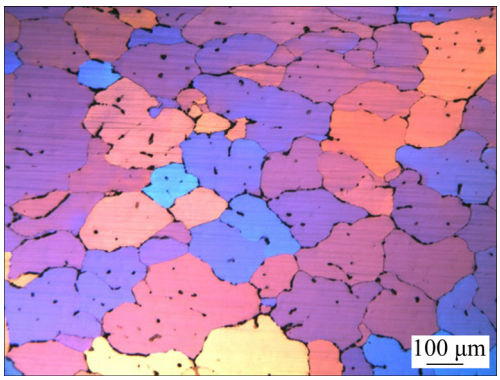

Fig. 1 Microstructure of homogenized alloy

finally compressed to 60% thickness reduction. After isothermal plane-strain compression testing, the compressed specimens were rapidly water quenched to obtain the microstructure at the corresponding test temperatures. The macro-morphology of the samples before and after deformation is presented in Fig. 2. No microcracks are detectable when the specimens are compressed at 400 °C, 1 s^{-1}; 420 °C, 0.1 s^{-1}; 480 °C, 0.1 s^{-1}; and 500 °C, 0.1 s^{-1}. Interestingly, the sample compressed at 500 °C, 0.01 s^{-1} is found to present obvious microcrack.

To meet the needs of microstructural observations, the samples after compression were machined along the cross-section of the compression axis. The microstructure characterization of all the samples was monitored by a field emission gun-environmental scanning electron microscopy (FEG-SEM, FEI) device equipped with an HKL Channel 5 EBSD System for electron backscatter diffraction (EBSD) observation and a Libra 200 FE transmission electron microscope manipulated with accelerating voltage of 200 kV for transmission electron microscopy (TEM) observation. The specimens for metallographic observation were carefully polished with mechanical polishing and then etched with standard Keller's reagent. The specimens were electropolished in a 30 vol.% HNO_3 and 70 vol.% CH_3OH solution at −30 °C with a voltage of ~10 V and a current of ~100 mA for TEM analysis.

3 Results

3.1 Flow stress curves

Figure 3 shows the representative true stress−true strain curves of AA2195 aluminum alloy obtained under the selected experimental conditions. It can be seen that there is a rapid increase in flow stress with the increase of strain in the early stage of deformation due to the effect of strain hardening. The flow stress then decreases immediately from the peak and finally reaches a steady level, which may be associated with the occurrence of DRV and/or DRX. Additionally, the flow stress rises with the increased strain rate and decreased temperature.

Compared with the specimens deformed at 400−480 °C, the specimens deformed at 500 °C possess the lowest flow stress, which is indicative of strong softening. However, the flow stress of the specimens compressed at 500 °C, 0.01 s^{-1}, begins to experience a downward trend that occurs at a high strain beyond the value of 0.9, owing to the occurrence of cracks (Fig. 2).

3.2 Processing map

In the light of DMM, the PM pioneered by PRASAD et al [20−22] is established under various deformation conditions. The DMM theory suggests that the hot compression process of the material is actually a process of energy consumption. Therefore, the total power (P) applied to the material

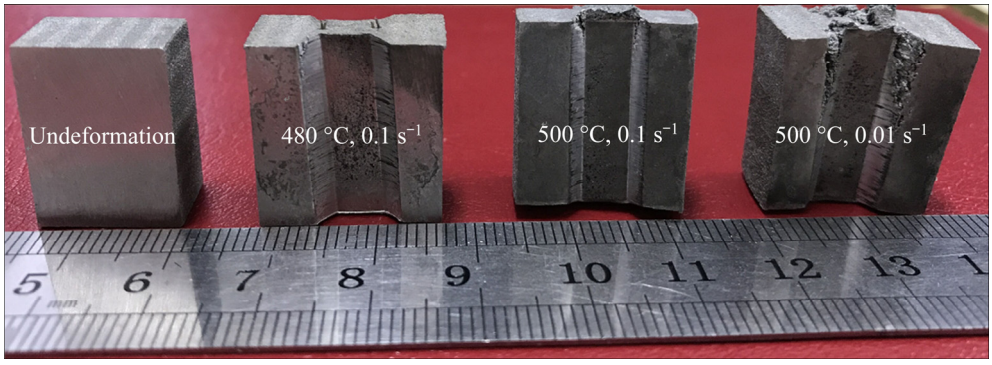

Fig. 2 Macro-morphologies of samples before and after compression

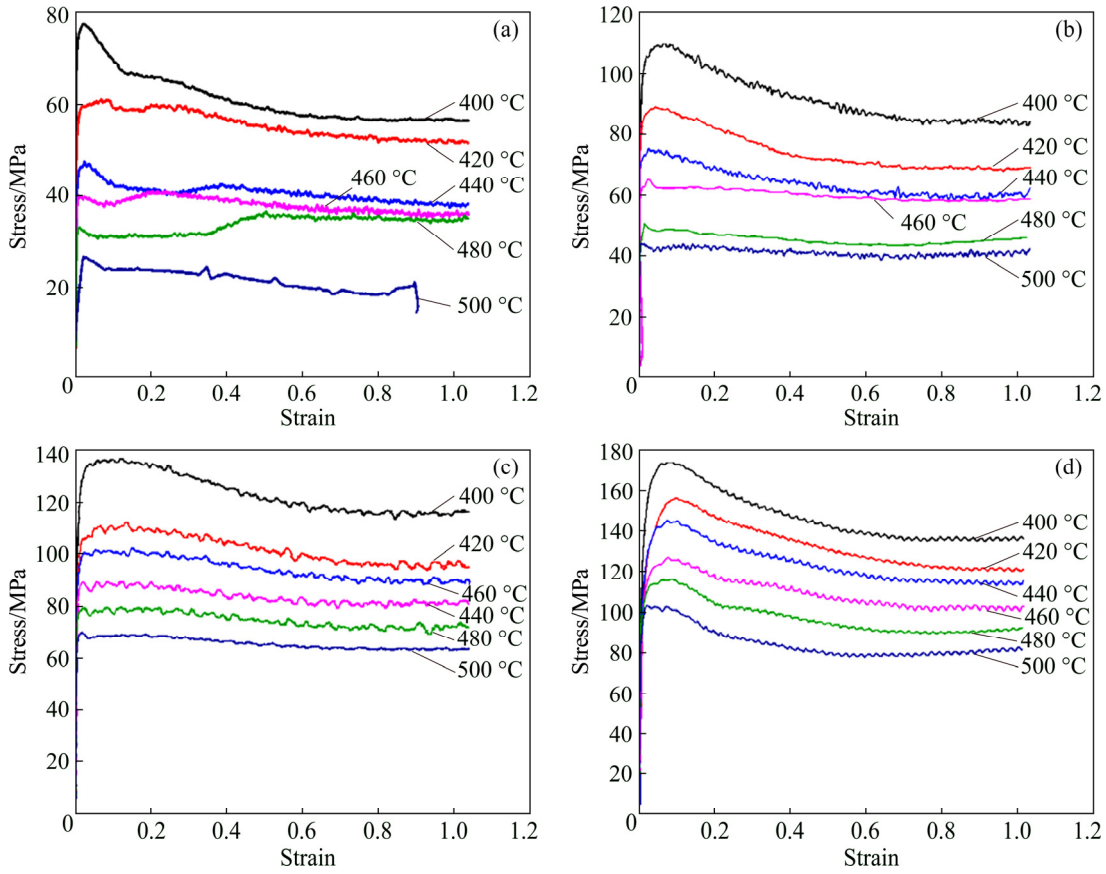

Fig. 3 Typical flow stress curves under various conditions for AA2195 aluminum alloy: (a) 0.01 s^{-1}; (b) 0.1 s^{-1}; (c) 1 s^{-1}; (d) 10 s^{-1}

consists of two complementary parts: G and J.

$$P = G + J = \int_0^{\dot{\varepsilon}} \sigma \mathrm{d}\dot{\varepsilon} + \int_0^{\sigma} \dot{\varepsilon} \mathrm{d}\sigma \tag{1}$$

where G is viscoplastic heat consumed in the hot compression process, J is the other part of the power that is dissipated through microstructural changes during hot compression such as DRV, DRX, phase transformations, super plasticity [23], pore as well as wedge cracks [14].

Under a given compression temperature and strain, the relationship between the flow stress and strain rate is represented by the constitutive equation:

$$\sigma = k\dot{\varepsilon}^{\mathrm{m}} \tag{2}$$

where k is a material parameter, $\dot{\varepsilon}$ is the strain rate, m is the strain rate sensitivity parameter.

The main parameters in the PM contain the strain rate sensitivity index (m) calculated by partial differential equations, and the efficiency of power dissipation (η) determined as a function of m. The non-dimensional parameter η is used for reflecting microstructural changes.

The m and η can be represented as follows:

$$m = \frac{\Delta \lg \sigma}{\Delta \lg \dot{\varepsilon}} \approx \frac{\dot{\varepsilon}\sigma \partial \ln \sigma}{\sigma \dot{\varepsilon} \partial \ln \dot{\varepsilon}} = \frac{\dot{\varepsilon} \partial \sigma}{\sigma \partial \dot{\varepsilon}} = \frac{\partial \ln \sigma}{\partial \ln \dot{\varepsilon}} = \frac{\partial J}{\partial G} \tag{3}$$

$$\eta = \frac{J}{J_{\max}} = \frac{2m}{m+1} \tag{4}$$

In Eqs. (3) and (4), for an ideal linear dissipation process, m is equal to 1. At the same time, $J_{\max}$ is the maximum value of J and it is calculated as $J_{\max}=\sigma\dot{\varepsilon}/2$.

In general, the instability map and the power dissipation map constitute PM by using flow stress data which were acquired from plane-strain compression tests.

The instability map is obtained by the different ξ with different T and $\dot{\varepsilon}$. In the light of extremum principles of irreversible thermodynamics, PRASAD et al [20,22] developed an unstable criterion applied to different metallic materials. The criterion of flow instability is represented as follows:

$$\xi(\dot{\varepsilon}) = \frac{\partial \ln[m/(m+1)]}{\partial \ln \dot{\varepsilon}} + m \le 0 \tag{5}$$

If the conditions satisfy Eq. (5), the undesirable microstructure may be observed, containing flow localization, twinning, dynamic strain aging, adiabatic shear band, kink bands, and so on. This typical metallurgical microstructure has an adverse influence on the manufacturing process of metal materials.

The power dissipation map is depicted by the variational η which is determined as a function of different T and $\dot{\varepsilon}$. This map shows different domains that undergo different metallurgical processes.

Figure 4 illustrates the established PM of AA2195 aluminum alloy at strain of 0.7 during hot compression. The figures beside each contour line in PM represent the different values of η. The shadow regimes stand for the unsafe conditions which satisfy the criterion of Eq. (5). Compared with other aluminum alloys, the instability regions of AA2195 aluminum alloy are much wider, appearing in Regime I (400−500 °C, 1−10 s^{-1}) and Regime II (400−430 °C, 0.01−1 s^{-1} and 430−460 °C, 0.04−1 s^{-1}). According to the previous studies [11], dynamic precipitation of T_1-Al_2CuLi phases occurred at low deformation temperatures (400−440 °C). T_1 precipitates with a high aspect ratio, the thin plate-shaped phases appearing on the matrix {111} planes, are the main strengthening precipitates in AA2195 aluminum alloy during artificial aging. These massive T_1-Al_2CuLi phases, the main precipitated phases, are also a significant barrier to inhibit DRV during hot deformation, which is unfavorable to the processing of aluminum alloy. Therefore, it is reasonable to assume that massive instability regions shown in Fig. 4 are attributed to the dynamic precipitation (T_1-Al_2CuLi phases), but further studies are needed to figure out what is the exact reason.

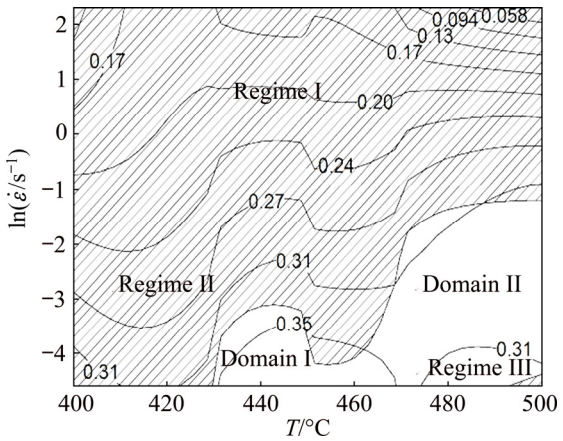

Fig. 4 Established PM of AA2195 aluminum alloy at strain of 0.7

The stability regions exist in Domain I (435−450 °C, 0.01−0.03 s^{-1}) which experiences a maximal efficiency of 0.39 close to 450 °C, 0.01 s^{-1} and Domain II (475−500 °C, 0.01−0.1 s^{-1} with the exception of 490−500 °C, 0.01 s^{-1}) which has a maximal efficiency of 0.35 close to 490 °C, 0.01 s^{-1}.

Interestingly, an easily overlooked small triangle instability domain, occurring at 490−500 °C, 0.01 s^{-1} in Regime III, can be observed at the lower right-hand side corner of PM, which shows a tendency to increase with the rise of temperature.

3.3 Microstructures

Figure 5 illustrates the typical EBSD images of the compressed specimens close to the triangle

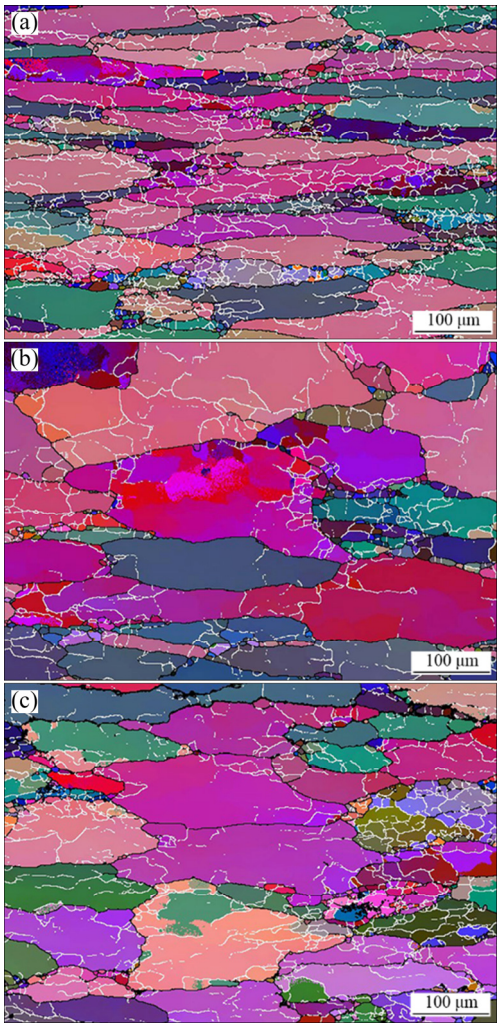

Fig. 5 EBSD images of specimens near Regime III: (a) 480 °C, 0.1 s^{-1}; (b) 500 °C, 0.1 s^{-1}; (c) 500 °C, 0.01 s^{-1}

domain (Regime III) at 480 °C, 0.1 s^{-1}; 500 °C, 0.1 s^{-1}; and 500 °C, 0.01 s^{-1}. In these EBSD images, the black lines denote high-angle boundaries having misorientation larger than 15° and the white lines denote low-angle boundaries having misorientation 2°−15°. The microstructure of all specimens close to Regime III contains a large number of elongated grains and a lot of fine recrystallized grains, which is the partially recrystallized microstructure. Although new quasi-equiaxed grains are observed, the fraction of high-angle grain boundaries is relatively low and dense dislocation substructures occur in the stretched grains, illustrating that both DRV and DRX are generated in the process of hot compression at high temperatures, but DRV is the dominant deformation mechanism. At 480 °C, 0.1 s^{-1}, the average size of recrystallization nuclei is about 5 μm. The size of recrystallized grain/subgrain and temperature increase and the strain rate decreases. The main reasons may be as follows: 1) High temperatures and low strain rates mean higher migration rates of high-angle grain boundaries and more time for recrystallization respectively. The growth of recrystallized nuclei occurs easily; 2) The subgrain rotation and coalescence are also thermally activated because of the high migration rate of atoms and dislocations; 3) DRX occurs by thermal activation. The nucleation rate increases as the deformation temperature increases. Therefore, compared with the specimens compressed at 480 °C, 0.1 s^{-1} and 500 °C, 0.1 s^{-1}, those compressed at 500 °C, 0.01 s^{-1} have a perfect softening effect.

As shown in Fig. 6, the configurations of dislocations (Figs. 6(a)−(c)), substructures (Figs. 6(a) and (b)) and DRX (Fig. 6(d)) of AA2195 aluminum alloy compressed at (480 °C, 0.1 s^{-1}) and (500 °C, 0.01 s^{-1}) are characterized by TEM. Dislocation walls (DWs) are formed (Figs. 6(b) and (c)), which is ascribed to dislocation climbing and sliding. At the same time, the disappearance of subgrain boundaries (SBs) contributes to the coalescence of the subgrains (Fig. 6(b)), resulting in a large quantity of fine continuous dynamic

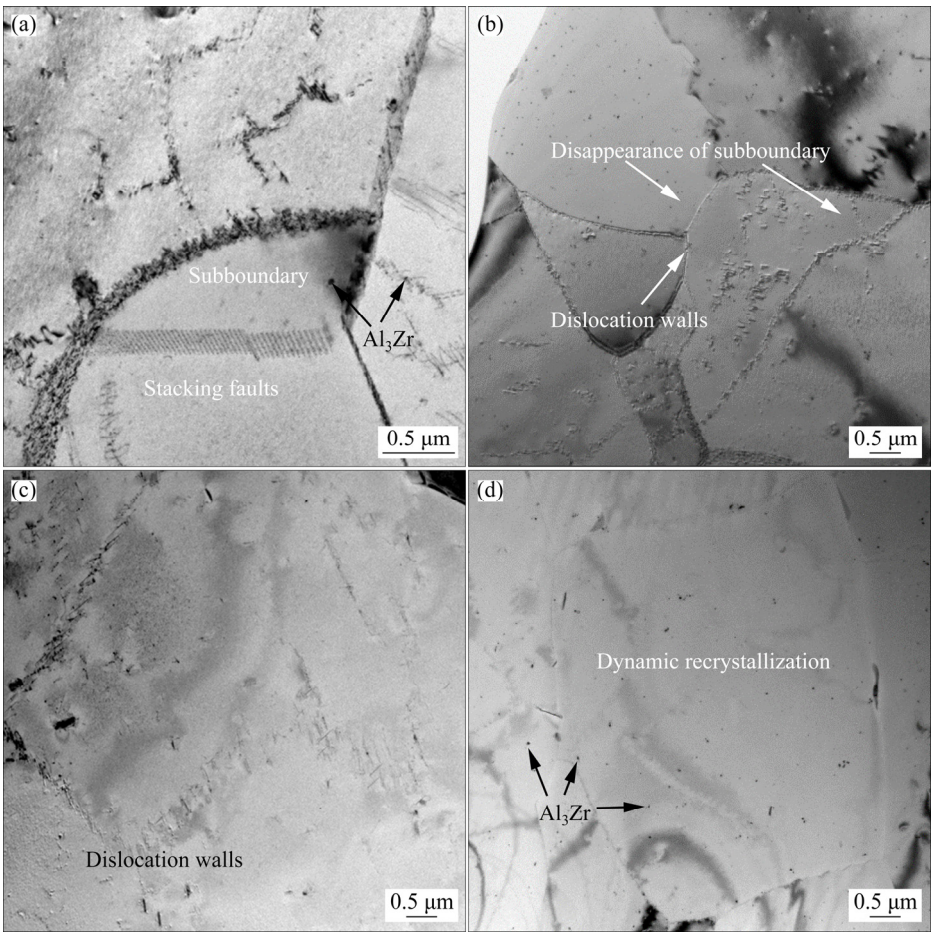

Fig. 6 Configurations of dislocations, substructures and DRX of AA2195 alloy compressed under different conditions: (a, b) 480 °C, 0.1 s^{-1}; (c, d) 500 °C, 0.01 s^{-1}

recrystallization (CDRX), as shown in Fig. 6(d). Therefore, the presence of DWs, subgrains and recrystallized grains reveals that both DRV and DRX exist during hot compression for all specimens deformed near Regime III.

When the temperature goes up and the strain rate falls down, the extent of DRV increases and the DRX takes place more sufficiently, which is consistent with the decrease of flow stress presented in Fig. 3.

Figure 7 shows the Al_3Zr dispersoids of AA2195 aluminum alloy under various compression

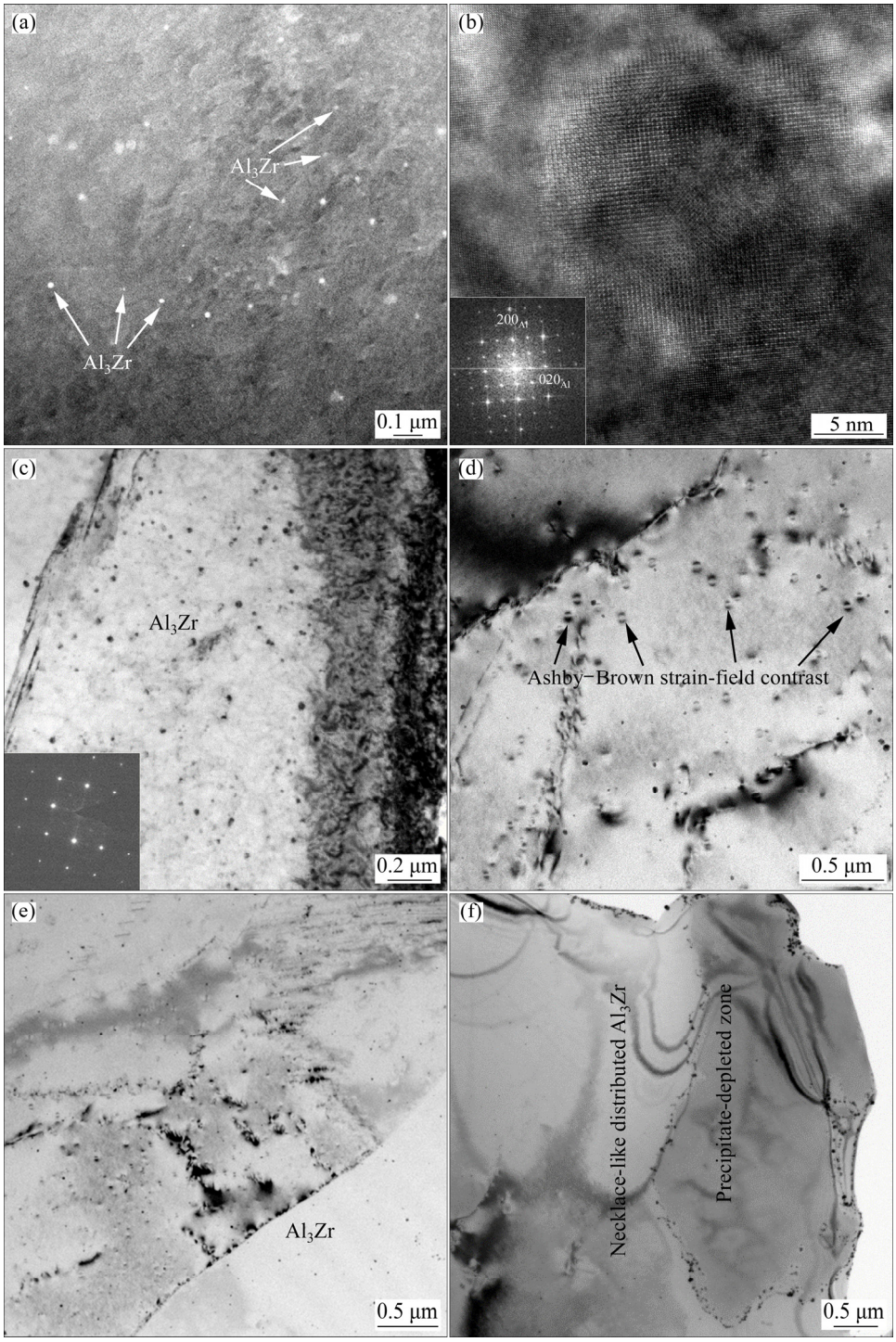

Fig. 7 TEM microstructures of Al_3Zr dispersoids for AA2195 aluminum alloy under various compression conditions: (a) HAADF-STEM image of homogenized alloys taken along $[001]_{Al}$; (b) HREM image, corresponding FFT patterns of homogenized alloys taken near $[001]_{Al}$; (c) BF image and corresponding SAD pattern (insert) taken near $[001]_{Al}$ at 480 °C, 0.1 s^{-1}; (d, e) BF images at 500 °C, 0.1 s^{-1}; (f) BF image at 500 °C, 0.01 s^{-1}

conditions at elevated temperatures. High-angle annular dark field scanning transmission electron microscopy (HAADF-STEM) image (Fig. 7(a)) taken along $[001]_{Al}$ shows the initial state of spheroidal Al_3Zr dispersoids with a mean diameter of ~27 nm in the non-deformed samples (the homogenized alloys). The HREM image and corresponding fast Fourier transform (FFT) patterns (Fig. 7(b)) of the homogenized samples give evidence of the metastable $L1_2$ Al_3Zr particles precipitated from the supersaturated solution because of low equilibrium solubility of Zr in Al matrix [6]. These particles are distributed homogeneously in the matrix of the homogenized alloys. BF image and corresponding SAD pattern (insert), recorded near $[001]_{Al}$ zone axis of the samples compressed at 480 °C, 0.1 s^{-1} are presented in Fig. 7(c). The $L1_2$-structured Al_3Zr particles with a mean diameter of ~30 nm are relatively stable during hot deformation at 480 °C, 0.1 s^{-1}. It is accepted that Cu and Ag can efficiently stabilize the metastable Al_3Zr particles [9]. Moreover, compared with the alloying elements such as Li, Cu, Mg and Ag, the heavy rare-earth element Zr possesses relatively low diffusion activation energy in aluminum. As a result, the $L1_2$ Al_3Zr particles show intrinsically coarsening resistance and homogeneous distribution in the Al matrix at high temperatures.

As the samples are compressed at high temperature, i.e. 500 °C, 0.1 s^{-1}, the spheroidal $L1_2$ particles (with a mean diameter of ~41 nm) obviously show the Ashby−Brown strain-field contrast-structural faults (Fig. 7(d)) in the interior of grains [6,24−28]. These structural faults can act as the diffusion path for Zr elements, leading to a further coarsening of Al_3Zr particles. Moreover, Al_3Zr particles are also re-precipitated along grain boundaries with the aid of the diffusion of Zr, as shown in Fig. 7(e), which also suggests that a portion of $L1_2$-structured Al_3Zr particles are locally dissolved into the matrix. SHI and CHEN [12] indicated that the nonequilibrium segregation of Zr in the dendrite centers during casting contributed to the heterogeneous distribution of Al_3Zr dispersoids near grain boundaries during solution treatment. Nevertheless, as reported by NES [29], the metastable Al_3Zr particles were no longer stable during hot deformation and dissolved discontinuously at the migrating boundaries, and then re-precipitated near the grain boundaries. In the present study, the segregation of Al_3Zr dispersoids near the grain boundaries is not observed under other deformation conditions such as 480 °C, 0.1 s^{-1}. Therefore, the segregation phenomena of Al_3Zr dispersoids cannot be interpreted by the theory of SHI and CHEN [12] but can be in good agreement with the earlier work by NES [29]. However, the repeated precipitation phenomena are only observed at a small part of grain boundaries, which can be attributed to insufficient compression time for the diffusion of Zr.

The average size of Al_3Zr particles under various compression conditions is listed in Table 2. It is clear that, compared with homogenized samples, the average particle size slightly increases at 480 °C, 0.1 s^{-1}, but rapidly increases with increasing temperature and decreasing strain rate of 500 °C, 0.1 s^{-1} and 500 °C, 0.01 s^{-1}. Because $L1_2$-structured particles develop Ashby−Brown strain-field contrast and begin to coarsen, the new Al_3Zr particles re-precipitate at a small part of grain boundaries during hot deformation at 500 °C.

Table 2 Average size of Al_3Zr particles under various compression conditions

Condition	Diameter/nm
Homogenized	27±1
480 °C, 0.1 s^{-1}	30±1
500 °C, 0.1 s^{-1}	41±3
500 °C, 0.01 s^{-1}	48±3

When the strain rate drops from 0.1 to 0.01 s^{-1} at 500 °C, an enormous precipitate-free zone is observed in the matrix (Fig. 7(f)), which is indicative of the dissolution of Al_3Zr particles in the Al matrix. At the same time, the Al_3Zr particles re-precipitate along grain boundaries, just like a necklace, as shown in Fig. 7(f). These phenomena can be attributed to the sufficient deformation time at elevated temperatures for the dissolution of Al_3Zr particles and rapid diffusion of Zr through the pipe of the grain boundary.

4 Discussion

In the present study, a large number of DWs and SBs (Fig. 6), as well as fine recrystallized grains (Fig. 5) are generated during hot deformation at elevated temperatures because of the absence of

T_1 precipitates (Fig. 6), which is in agreement with the results by YANG et al [30]. Therefore, the predominant restoration mechanisms are DRV accompanied by fine recrystallized grains during hot compression at high temperatures.

However, hindrance caused by Al_3Zr particles still plays a major role in DRV and DRX at 480 °C and 500 °C. Figure 8 shows TEM images of the influence of Al_3Zr particles on the microstructure for AA2195 aluminum alloy. The dislocations are pinned by the particles, increasing the difficulty in the polygonization of the dislocations. Simultaneously, these particles also restrict DRX grain growth by inhibiting the migration of grain boundaries (Figs. 6(d) and 8(b)). These phenomena are consistent with the fibrous microstructures and fine recrystallized grains observed from EBSD images, as shown in Fig. 5.

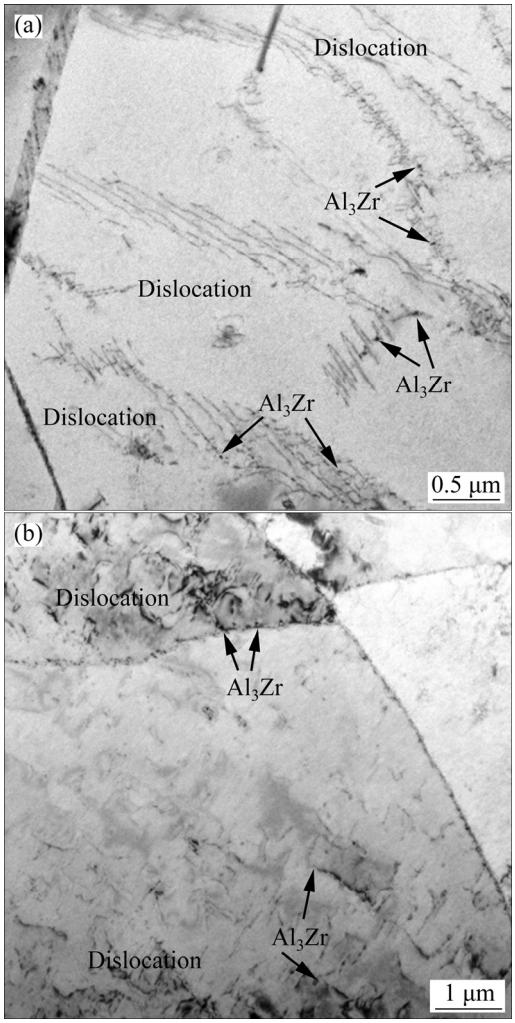

Fig. 8 TEM images showing influence of Al_3Zr particles on microstructure for AA2195 aluminum alloy compressed under different conditions: (a) 480 °C, 0.1 s^{-1}; (b) 500 °C, 0.01 s^{-1}

As AA2195 aluminum alloy is compressed at 480 °C, 0.1 s^{-1}, the Al_3Z particles exhibit good coarsening resistance (Fig. 7(c) and Table 2), and can effectively restrain the polygonization of the dislocations and recrystallized grains growth. Therefore, Al_3Z particles are an important barrier for DRV and recrystallized grains growth.

When the temperature increases to 500 °C, the Al_3Zr particles partially coarsen and then transform into the transitional Al_3Zr particles, or partially dissolve into the matrix and subsequently re-precipitate along grain boundaries during the hot compression process. The coarseness and dissolution of Al_3Zr particles result in weak pinning of dislocations and boundaries. Therefore, the extent of DRV and DRX increases, which is consistent with the features of stability domains of PM. Simultaneously, the efficiency of the power dissipation of the instability region (Regime III) is ~0.41, which is associated with DRX process [19]. However, the small triangle instability domain (Regime III) at 490−500 °C, 0.01 s^{-1} (Fig. 4) and macroscopic cracks on the surface of the samples compressed at 500 °C, 0.01 s^{-1} (Fig. 2) indicate that the specimens manifest the poor workability of AA2195 aluminum alloy.

Different explanations are proposed to account for the macroscopic cracks of the specimens deformed at 500 °C, 0.01 s^{-1} (Regime III) (Fig. 2). The first possibility is that the poisoning effect of Zr contributes to coarse grain structures [12]. However, the re-precipitation phenomena near the grain boundaries can effectively reduce Zr content in the matrix. The second explanation is that a large number of necklace-like distributed Al_3Zr particles spreading along the grain boundaries (Fig. 7(f)) reduce the bond strength of grain boundaries and ultimately generate cavity along the grain boundary. Meanwhile, the cracking behavior is also detectable for intergranular cracking when the specimens of 2195 aluminum alloy are compressed at 500 and 550 °C [17]. The brittle intergranular cracking of 2195 aluminum alloy indicates the decrease of bonding strength of grain boundaries. Therefore, the necklace-like distributed Al_3Zr particles are responsible for macroscopic cracks of AA2195 aluminum alloy at high temperatures.

As the temperature rises, the diffusion rate of Zr increases [31−33]. Therefore, the specimens deformed at the high temperature (500 °C) show

macroscopic cracks (Fig. 2). Moreover, the small triangle instability domain (Regime III) at 490−500 °C, 0.01 s^{-1} shows a tendency to increase with the increase of temperature (Fig. 4). Simultaneously, the diffusion of Zr needs sufficient time to complete because of the low diffusion rate of Zr. Consequently, fracture occurs only at a high strain level beyond the true strain of ~0.9.

This study has shown that although Regime III (490−500 °C, 0.01 s^{-1}) possesses a perfect softening effect, this instability domain should be avoided in processing.

5 Conclusions

(1) As the specimens are deformed at 480 °C, 0.1 s^{-1}, the metastable Al_3Zr particles are relatively stable and effectively impede DRV and DRX grain growth.

(2) As the specimens are deformed at 500 °C, the Al_3Zr particles rapidly coarsen into the transitional Al_3Zr particles or dissolve and re-precipitate along grain boundaries. The coarseness and dissolution of Al_3Zr particles are favorable to DRV and DRX.

(3) The necklace-like distributed Al_3Zr particles along the grain boundary are attributed to the local dissolution of Al_3Zr particles and the rapid diffusion of Zr through the pipe of the grain boundary, which results in an easily overlooked small triangle instability domain at 490−500 °C, 0.01 s^{-1} in PM and macroscopic cracks on sample surface.

References

[1] PICKENS J R. Recent developments in the weldability of lithium-containing aluminum alloys [J]. Journal of Materials Science, 1990, 25: 3035−3047.

[2] WILLIAMS J C, STARKE E A. Progress in structural materials for aerospace systems [J]. Acta Materialia, 2003, 51: 5775−5799.

[3] RIOJA R J. Fabrication methods to manufacture isotropic Al−Li alloys and products for space and aerospace applications [J]. Materials Science and Engineering A, 1998, 257: 100−107.

[4] LI Hong-ying, GAO Zhao-he, YIN Hao, JIANG Hao-fan, SU Xiong-jie, BIN Jie. Effects of Er and Zr additions on precipitation and recrystallization of pure aluminum [J]. Scripta Materialia, 2013, 68: 59−62.

[5] TSIVOULAS D, ROBSON J D. Heterogeneous Zr solute segregation and Al_3Zr dispersoid distributions in Al−Cu−Li alloys [J]. Acta Materialia, 2015, 93: 73−86.

[6] KNIPLING K E, DUNNAND D C, SEIDMAN D N. Precipitation evolution in Al−Zr and Al−Zr−Ti alloys during aging at 450−600 °C [J]. Acta Materialia, 2008, 56: 1182−1195.

[7] KNIPLING K E, DUNNAND D C, SEIDMAN D N. Precipitation evolution in Al−Zr and Al−Zr−Ti alloys during isothermal aging at 375−425 °C [J]. Acta Materialia, 2008, 56: 114−127.

[8] LI Hong-ying, BIN Jie, LIU Jiao-jiao, GAO Zhao-he, LU Xiao-chao. Precipitation evolution and coarsening resistance at 400 °C of Al microalloyed with Zr and Er [J]. Scripta Materialia, 2012, 67: 73−76.

[9] HU Hai, ZHAO Ming-qi, WU Xiao-zhi, JIA Zhi-hong, WANG Rui, LI Wei-guo, LIU Qing. The structural stability, mechanical properties and stacking fault energy of Al_3Zr precipitates in Al−Cu−Zr alloys: HRTEM observations and first-principles calculations [J]. Journal of Alloys and Compounds, 2016, 681: 96−108.

[10] SCHWARZ R B, DESCH P B, SRINIVASAN S, NASH P. Synthesis and properties of trialuminides with ultra-fine microstructures [J]. Nanostructured Materials, 1992, 1: 37−42.

[11] AVRAMOVIC-CINGARA G, PEROVIC D D, MCQUEEN H J. Hot deformation mechanisms of a solution-treated Al−Li−Cu−Mg−Zr alloy [J]. Metallurgical and Materials Transactions A, 1996, 27: 3478−3490.

[12] SHI C J, CHEN X G. Effect of Zr addition on hot deformation behavior and microstructural evolution of AA7150 aluminum alloy [J]. Materials Science and Engineering A, 2014, 596: 183−193.

[13] KRIDLI G T, EL-GIZAWY A S, LEDERICH R. Development of process maps for superplastic forming of Weldalite™ 049 [J]. Materials Science and Engineering A, 1998, 244: 224−232.

[14] REDDY G J, SRINIVASAN N, GOKHALE A A, KASHYAP B P. Processing map for hot working of spray formed and hot isostatically pressed Al−Li alloy (UL40) [J]. Journal of Materials Processing Technology, 2009, 209: 5964−5972.

[15] OU Liu, ZHENG Zi-qiao, NIE Yu-feng, JIAN Hai-gen. Hot deformation behavior of 2060 alloy [J]. Journal of Alloys and Compounds, 2015, 648: 681−689.

[16] HE Hai-lin, YI You-ping, CUI Jin-dong, HUANG Shi-quan. Hot deformation characteristics and processing parameter optimization of 2219 Al alloy using constitutive equation and processing map [J]. Vacuum, 2019, 160: 293−302.

[17] WANG Yong-xiao, ZHAO Guo-qun, XU Xiao, CHEN Xiao-xu, ZHANG Cun-sheng, Constitutive modeling, processing map establishment and microstructure analysis of spray deposited Al−Cu−Li alloy 2195 [J]. Journal of Alloys and Compounds, 2019, 779: 735−751.

[18] LI Bo, PAN Qing-lin, YIN Zhi-min. Characterization of hot deformation behavior of as-homogenized Al−Cu−Li−Sc−Zr alloy using processing maps [J]. Materials Science and Engineering A, 2014, 614: 199−206.

[19] YIN Hao, LI Hong-ying, SU Xiong-jie, HUANG De-sheng. Processing maps and microstructural evolution of isothermal compressed Al−Cu−Li alloy [J]. Materials Science and Engineering A, 2013, 586: 115−122.

[20] PRASAD Y V R K, GEGEL H L, DORAIVELU S M, MALAS J C, MORGAN J T. Modeling of dynamic material behavior in hot deformation: Forging of Ti-6242 [J]. Metallurgical Transactions A, 1984, 15: 1883−1892.
[21] PRASAD Y V R K, SESHACHARYULU T. Modelling of hot deformation for microstructural control [J]. International Materials Reviews, 2013, 43: 243−258.
[22] PRASAD Y V R K, SESHACHARYULU T. Processing maps for hot working of titanium alloys [J]. Materials Science and Engineering A, 1998, 243: 82−88.
[23] EDDAHBI M, THOMSON C B, CARRENO F, RUNAO O A. Grain structure and microtexture after high temperature deformation of an Al−Li (8090) alloy [J]. Materials Science and Engineering A, 2000, 284: 292−300.
[24] CHEN Y C, FINE M E, WEETMAN J R. Microstructural evolution and mechanical properties of rapidly solidified Al−Zr−V alloys at high temperatures [J]. Acta Metallurgica et Materialia, 1990, 38: 771−780.
[25] CHEN Y C, FINE M E, WEETMAN J R, LEWI R E. Coarsening behavior of Ll_2 structured $Al_3(Zr_xV_{1-x})$ precipitates in rapidly solidified Al−Zr−V alloy [J]. Scripta Materialia, 1987, 21: 1003−1008.
[26] LAASRAOUI A, JONAS J J. Prediction of steel flow stresses at high temperatures and strain rates [J]. Metallurgical Transactions A, 1991, 22: 1545−1558.
[27] LEE H, HAN S Z, LEE H M, LEE Z H. Coarsening behavior of $L1_2$ precipitates in melt-spun Al−Ti−V−Zr alloys [J]. Materials Science and Engineering A, 1993, 163: 81−90.
[28] ZEDALIS M S, FINE M E. Precipitation and ostwald ripening in dilute Al base-Zr−V alloys [J]. Metallurgical Transactions A, 1986, 17: 2187−2198.
[29] NES E. Hot deformation behaviour of particle-stabilized structures in Zr-bearing Al alloys [J]. Metal Science, 1979, 13: 211−215.
[30] YANG Qing-bo, WANG Xin-zhu, LI Xu, DENG Zan-hui, JIA Zhi-hong, ZHANG Zhi-qing, HUANG Guang-jie, LIU Qing. Hot deformation behavior and microstructure of AA2195 alloy under plane strain compression [J]. Materials Characterization, 2017, 131: 500−507.
[31] JIA Zhi-hong, RØYSET J, SOLBERG J K, LIU Qing. Formation of precipitates and recrystallization resistance in Al−Sc−Zr alloys [J]. Transactions of Nonferrous Metals Society of China, 2012, 22: 1866−1871.
[32] PENG Yong-yi, YIN Zhi-min, NIE Bo, ZHONG Li. Effect of minor Sc and Zr on superplasticity of Al−Mg−Mn alloys [J]. Transactions of Nonferrous Metals Society of China, 2007, 17: 744−750.
[33] LIN Hua-qiang YE Ling-ying, SUN Lin, XIAO Tao, LIU Sheng-dan, DENG Yun-lai, ZHANG Xin-ming. Effect of three-step homogenization on microstructure and properties of 7N01 aluminum alloys [J]. Transactions of Nonferrous Metals Society of China, 2018, 28: 829−838.

高温下 Al_3Zr 颗粒对 Al−Cu−Li 基合金的热变形行为以及加工图的影响

杨庆波[1]，邓燕君[2]，杨 谋[1]，张志清[1,3,4]，李卫国[5]，刘 庆[1]

1. 重庆大学 材料科学与工程学院，重庆 400045；
2. 长安汽车工程研究总院，重庆 401120；
3. 中国西彭铝业工业园，重庆 401326；
4. 重庆大学 重庆大学−辛辛那提大学联合学院，重庆 401331；
5. 重庆大学 航空航天学院，重庆 400045

摘 要：采用等温平面压缩试验研究 Al_3Zr 颗粒在不同温度(400~500 °C)以及应变速率(0.01~10 s^{-1})条件下对 Al−Cu−Li 基合金热压缩行为以及加工图的影响。通过金相观察(OM)、电子背散射衍射(EBSD)以及透射电镜(TEM)系统地表征不同变形条件下合金的显微组织。结果表明，在软化过程中相对于动态再结晶，动态回复起主导作用。在低温条件下，亚稳态 Al_3Zr 颗粒能够有效抑制动态回复以及动态再结晶的长大。当温度达到 500 °C 时，晶界附近的 Al_3Zr 颗粒发生熔解，随 Zr 元素在晶界快速扩散，Al_3Zr 颗粒在晶界再次析出，并呈链状分布。这些链状分布的 Al_3Zr 颗粒在热变形过程中导致宏观裂纹，在加工图中形成不安全区域(490~500 °C，0.01 s^{-1})。

关键词：Al−Cu−Li 基合金；Al_3Zr 颗粒；热压缩；加工图

(Edited by Xiang-qun LI)